# Direct Ink Writing of 3D Functional Materials**

By *Jennifer A. Lewis**

The ability to pattern materials in three dimensions is critical for several technological applications, including composites, microfluidics, photonics, and tissue engineering. Direct-write assembly allows one to design and rapidly fabricate materials in complex 3D shapes without the need for expensive tooling, dies, or lithographic masks. Here, recent advances in direct ink writing are reviewed with an emphasis on the push towards finer feature sizes. Opportunities and challenges associated with direct ink writing are also highlighted.

5 µm
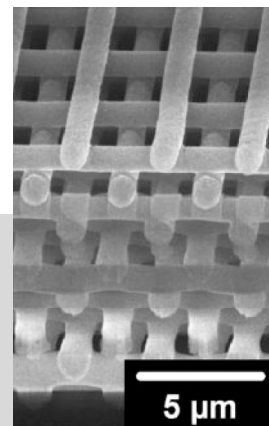
1. Introduction

New methods for materials fabrication at the micro- and nanoscale will drive scientific and technological advances in areas of materials science, chemistry, physics, and biology. The broad diversity of potentially relevant materials, length scales, and architectures underscores the need for flexible patterning approaches. One important example is the fabrication of 3D periodic structures comprised of colloidal,[1] polymeric,[2–4] or semiconductor[5] materials. These structures may find potential application as sensors,[6] microfluidic networks,[7] photonic-bandgap materials,[8] tissue-engineering scaffolds,[9] and drug-delivery devices.[10] Several strategies have recently emerged for precisely assembling 3D periodic arrays,[1–5] including colloidal-epitaxy,[1] standard-lithographic,[5] and direct-write techniques.[2,4] Of these, only the latter approach offers the materials flexibility, low cost, and ability to construct arbitrary 3D structures required for advances across multidisciplinary boundaries.

The term "direct ink writing" describes fabrication methods that employ a computer-controlled translation stage, which moves a pattern-generating device, that is, an ink-deposition nozzle, to create materials with controlled architecture and composition.[11] Several direct ink writing techniques have been introduced that are capable of patterning materials in three dimensions. They can be divided into filamentary-based approaches, such as robocasting[12,13] (or robotic deposition[4,7,14,15]), micropen writing,[16] and fused deposition,[17,18] and droplet-based approaches, such as ink-jet printing,[19,20] and hot-melt printing[21] (see Fig. 1). Many ink designs have been employed including highly shear thinning colloidal suspensions,[12,13,16] colloidal gels,[15,22] polymer melts,[17] dilute colloidal fluids,[20] waxes,[21,23] and concentrated polyelectrolyte complexes.[4,24,25] These inks solidify either through liquid evaporation,[12,13,19,20] gelation,[7,14,15] or a temperature-[17,18] or solvent-induced phase change.[4,24,25]

Through careful control of ink composition, rheological behavior, and printing parameters, 3D structures that consist of continuous solids, high aspect ratio (e.g., parallel walls), or spanning features can be constructed. Of these, the latter structures offer the greatest challenge for designing inks, because they contain self-supporting features that must span gaps in the underlying layer(s). This feature article focuses primarily on our recent efforts to design concentrated colloidal,[15,22] fugitive organic,[23] and polyelectrolyte[4,24,25] inks for the direct ink writing of 3D periodic architectures with filamentary features ranging from hundreds of micrometers to sub-micrometer in size, and their respective applications as functional composites,[14] microfluidic networks,[7] and templates for photonic bandgap materials[26] and inorganic–organic hybrid structures.[25] Future opportunities and current challenges for this novel patterning approach are also highlighted.

[*] Prof. J. A. Lewis
Materials Science and Engineering Department
Frederick Seitz Materials Research Laboratory
University of Illinois at Urbana-Champaign
1304 W. Green St., Urbana, IL 61801 (USA)
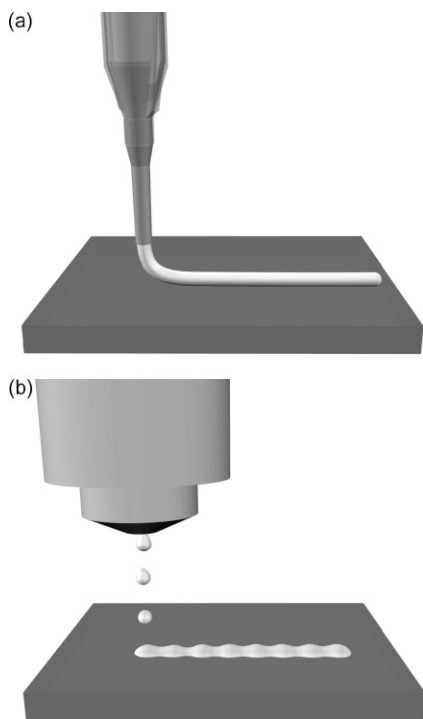E-mail: jalewis@uiuc.edu

Figure 1. Schematic illustration of direct ink writing techniques: a) continuous filament writing and b) droplet jetting. Adapted with permission from [11]. Copyright 2004 (Elsevier).

2. Colloidal Inks for Direct Writing of 3D Functional Composites

2.1. Ink Design and Rheology

Colloidal gels are excellent candidate materials for direct ink writing of complex 3D structures, because their viscoelastic properties can be tailored over many orders of magnitude to facilitate flow through nozzles and produce patterned filaments that maintain their shape, even as they span gaps in the underlying layers of the printed structure.[15,22] We designed these inks with two important criteria in mind. First, they must exhibit a well-controlled viscoelastic response, so they flow through the deposition nozzle and then "set" immediately to facilitate

shape retention of the deposited features even as they span gaps in the underlying layer(s). Second, they must contain a high colloid volume fraction to minimize drying-induced shrinkage after assembly is complete, so the particle network is able to resist compressive stresses arising from capillary tension.[27] These criteria required careful control of colloidal forces to first generate a highly concentrated, stable dispersion followed by inducing a system change (e.g., ΔpH, ionic strength, or solvent quality) that promotes the fluid-to-gel transition illustrated schematically in Figure 2a.

The colloid volume fraction (ϕ) of the ink is held constant, while its mechanical properties are tuned by tailoring the strength of the interparticle attraction according to the scaling relationship[28] given by

$$y = k\left(\frac{\phi}{\phi_{gel}} - 1\right)^x \tag{1}$$

where y is the mechanical property of interest (shear yield stress, τ_y, or elastic shear modulus, G'), k is a constant, ϕ_{gel} is the colloid volume fraction at the gel point, and x is the scaling exponent (ca. 2.5). The equilibrium mechanical properties of a colloidal gel are governed by two parameters: ϕ, which is proportional to the interparticle bond density, and ϕ_{gel}, which scales inversely with bond strength. As the attractive forces between particles strengthen, colloidal gels (of constant ϕ) experience a significant increase in both τ_y and G'.

Colloidal gels consist of a percolating network of attractive particles capable of transmitting stress above ϕ_{gel}. When stressed beyond their yield point (τ_y), they exhibit shear thinning flow behavior due to the attrition of particle–particle bonds within the gel, as described by[29]

$$\tau = \tau_y + K\dot{\gamma}^n \tag{2}$$

where τ is the shear stress, n is the shear thinning exponent (<1), K is the viscosity parameter, and $\dot{\gamma}$ is the shear rate. Gel-based inks flow with a three-zone velocity profile within the cylindrical deposition nozzle, which consists of an unyielded (gel) core moving at a constant velocity surrounded by a yielded (fluid) shell experiencing laminar flow and a thin slip layer devoid of colloidal particles at the nozzle wall.[30] The ink

Dr. Jennifer A. Lewis received a B.S. degree with high honors in ceramic engineering from the University of Illinois at Urbana-Champaign (UIUC) in 1986 followed by a Sc.D. in ceramic science from the Massachusetts Institute of Technology (MIT) in 1991. She joined the faculty of the materials science and engineering department at UIUC in 1990, where she is currently appointed as the Hans Thurnauer Professor of Materials Science and Engineering and the Interim Director of the Frederick Seitz Materials Research Laboratory. Her research interests focus primarily on the directed assembly of functional ceramic, microfluidic, photonic, and tissue-engineering structures from colloidal, nanoparticle, and polymeric building blocks.
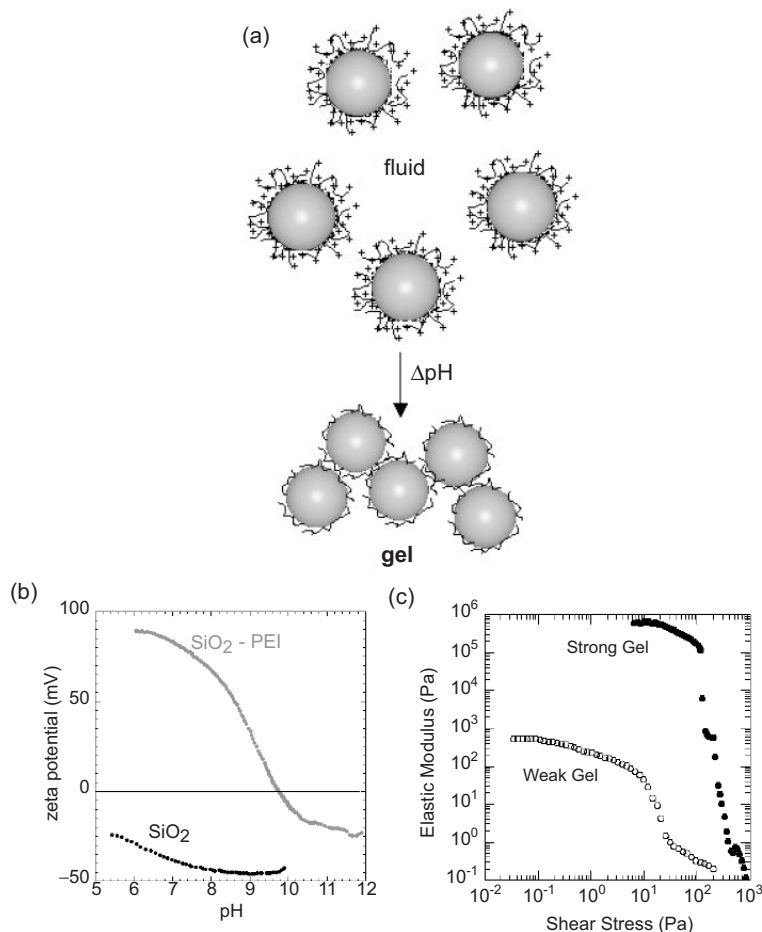
Figure 2. a) Schematic illustration of the fluid-to-gel transition observed for colloidal inks. b) Plot of zeta potential as a function of pH for PEI-coated silica (gray) and bare silica (black) microspheres suspended in water. c) Log–log plot of shear elastic modulus as a function of shear stress for concentrated silica gels of varying strength: open symbols denote weak gel (pH 9.5) and filled symbols denote strong gel (pH 9.75). [Note: The point-of-zero charge for PEI-coated silica microspheres occurs at pH 9.75, which is significantly above the value (pH 2–3) observed for bare silica particles. The weak gel had insufficient strength to support its own weight during deposition, whereas the strong gel could be successfully patterned into 3D periodic structures.] Reproduced with permission from [22].

exits the nozzle as a continuous, rodlike filament with a rigid (gel)-core/fluid-shell architecture, which simultaneously promotes shape retention and allows it to fuse with previously patterned features at contact points. Upon deposition, the fluid shell quickly transforms to a gelled state as the attractive particle bonds reform.[15]

2.2. Model Colloidal Inks for Direct-Write Assembly

We first demonstrated this ink design using a model system consisting of monosized silica spheres (1.17 μm diameter) coated with poly(ethylenimine) (PEI, weight-average molecular weight, $M_w = 2000$ g mol^{-1}, 0.5 mg PEI/m^2 silica) and suspended in deionized water.[22] Concentrated silica suspensions

($\phi = 0.46$) exhibited a fluid-to-gel transition as their pH was adjusted to a value near their point-of-zero charge, shown in Figure 2b. A dramatic rise in elastic properties accompanied this phase transition, as shown in Figure 2c. Both the shear yield stress and elastic modulus increased by orders of magnitude because of strengthened interparticle attractions near this pH value. Below τ_y, the system resides in the linear viscoelastic region and G' is independent of applied stress. Above τ_y, interparticle bonds begin to rupture leading to the sharp decrease in G', as observed in Figure 2c.

To demonstrate our approach, 3D periodic structures were assembled from this model colloidal ink. The ink was housed in a syringe (barrel diameter of 4.6 mm) mounted on the *z*-axis of a three-axis motion-controlled stage, and dispensed through a cylindrical deposition nozzle (250 μm in diameter) onto a moving *x–y* stage (velocity of 5 mm s^{-1}). The lattice structures produced (see Fig. 3) consist of a linear array of rods aligned with the *x*- or *y*-axis such that their orientation is orthogonal to the previous layer, with a rod spacing (*L*) of 250 μm. The top two layers of the 3D structure are shown in Figure 3a, alongside the corresponding height profile (Fig. 3b) acquired by noncontact laser profilometry. These data reveal the excellent height uniformity of the deposited features even as they span gaps in the underlying layer(s). The cross-sectional cut through the lattice shows that the rods maintain their cylindrical shape during the multilayer deposition process (see Fig. 3c). The higher magnification view of the rod surface, shown in Figure 3d, reveals the disordered nature of the colloidal gel-based ink used to fabricate such structures.[22] Note, the shape of these viscoelastic ink filaments conforms to the nozzle geometry, allowing one to print 3D structures composed of noncylindrical features (see Fig. 4).[31]

This ink design can be readily extended to any type of colloidal (or nanoparticulate) material, provided their interparticle forces can be controlled to produce the desired solids concentration and rheological properties. In addition to pH change, the requisite ink rheology may be achieved through the addition of salt[32] or oppositely charged polyelectrolyte species,[31] as recently demonstrated for nanoparticle and other colloidal inks, respectively. These strategies have been employed to produce inks from a broad array of colloidal materials, including silica,[22] lead zirconate titanate,[15] barium titanate,[32] alumina,[31] mullite,[33] silicon nitride,[34] and hydroxyapatite.[35]

2.3. Direct-Write Assembly of 3D Functional Composites

Interpenetrating phase composites, IPCs, composed of ferroelectric lead zirconate titanate (Pb(Zr$_{0.53}$Ti$_{0.47}$)O$_3$, PZT)
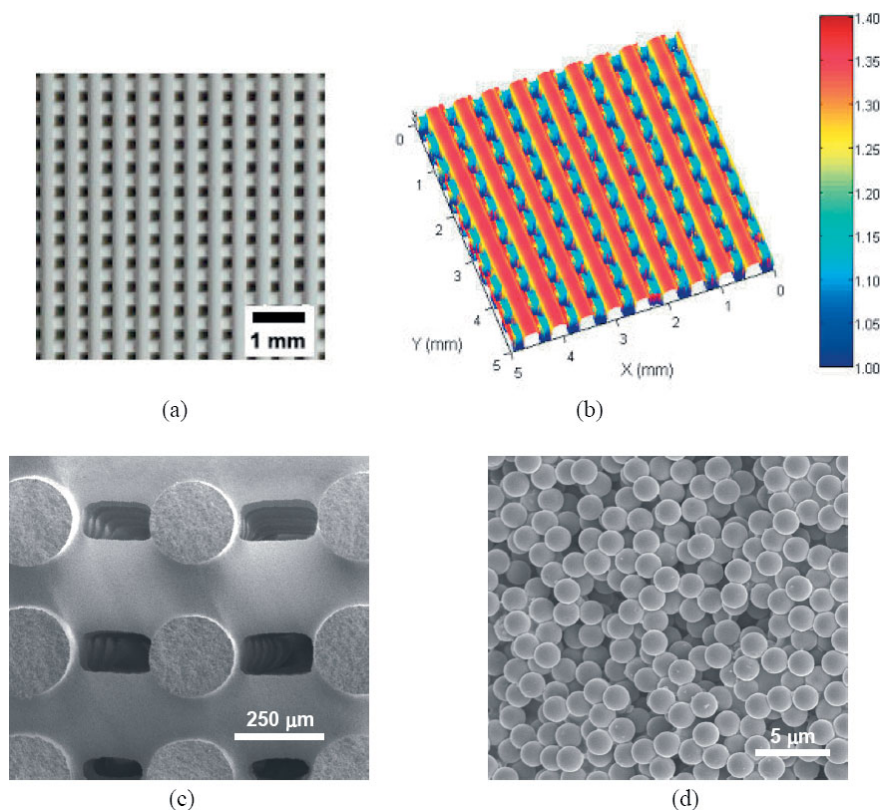
Figure 3. a) Optical microscopy image of a 3D periodic structure comprising a simple cubic geometry (10 layers, 250 μm rod diameter, 500 μm pitch) assembled from a concentrated colloidal silica gel-based ink (pH 9.75) and b) corresponding profilometry scan of their top surface, where layer 10 (red) and layer 9 (blue) are indicated by the accompanying color bars. c) Scanning electron microscopy (SEM) image of a cross-sectional cut through the 3D structure, which reveals that the deposited rods maintain their cylindrical shape upon deposition and drying. d) SEM image of the colloidal gel network that persists upon drying. Adapted with permission from [22].
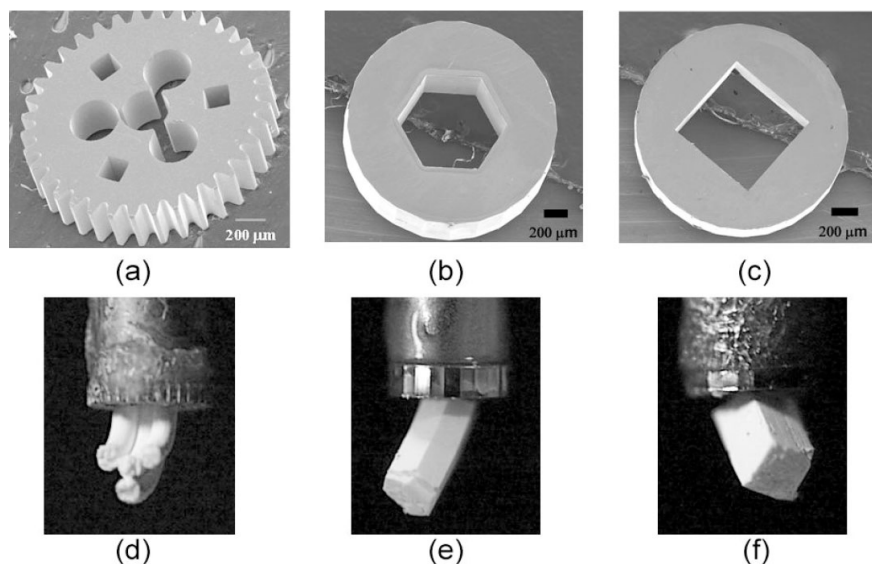

Figure 4. a) SEM images of the micro-designed nozzle tips: a) Lithography, Electroforming, Moulding (LIGA) gear, b) UV-LIGA μ-tip with a 560 μm vertex-to-vertex hexagonal orifice, and c) UV-LIGA μ-tip with a 745 μm (edge length) square orifice. d)–f) Corresponding optical images of ink filaments formed by extrusion through deposition nozzles modified with the attached microdesigned tips. Adapted with permission from [31].

and polymer are known to display high piezoelectric coefficients and low acoustic impedance, which makes them attractive for modern sonar and ultrasound systems. Their properties vary with the connectivity of the stiff ferroelectric and compliant polymer phases as well as the volume fraction of each phase. To explore these effects on their piezoelectric response, several 3D lattices were fabricated by direct writing a concentrated PZT ink ($\phi = 0.47$). We first produced the 3–3 structures shown in Figure 5a, in which both the ferroelectric and polymeric phases are interconnected in all three dimensions. Using this assembly route, the device architecture was varied rapidly simply by changing the printing pattern. For example, solid face-plates of PZT (see Fig. 5b) or solid face-plates with an outer PZT ring (see Fig. 5c) were added to the 3–3 structures to form 3–2 and 3–1 composites, respectively. In each case, the diameter of the PZT rods was fixed at ca. 160 μm, while their spacing in the *x–y* directions was systematically varied to yield PZT volume fractions ranging from 0.17 to 1. These skeletal PZT lattices were then sintered by heating them to 1300 °C for 2 h. After densification, the intervening pore space between the PZT rods was infiltrated with an epoxy resin. The composites and monolithic PZT disks were then polished, had electrodes deposited by gold sputtering, and then poled at 25 V cm^{-1} for 30 min at room temperature followed by short-circuiting for 1 h to accelerate aging. Finally, their dielectric constant and hydrostatic piezoelectric response were measured.[36]

The enhancement of the hydrostatic figure of merit ($\bar{d}_h\bar{g}_h$) of each composite is illustrated in Figure 5d. The 3–1 composites exhibited a 70-fold increase above that of monolithic PZT owing to a dramatically reduced dielectric constant and maintenance of a high piezoelectric response at 40 vol % PZT.[14] Our approach can be readily extended to a broad range of composite architectures, materials, and target applications, including other functional composites, structural composites (e.g., alumina/aluminum IPCs[37]), and bone scaffolds (e.g., hydroxyapatite[35]).
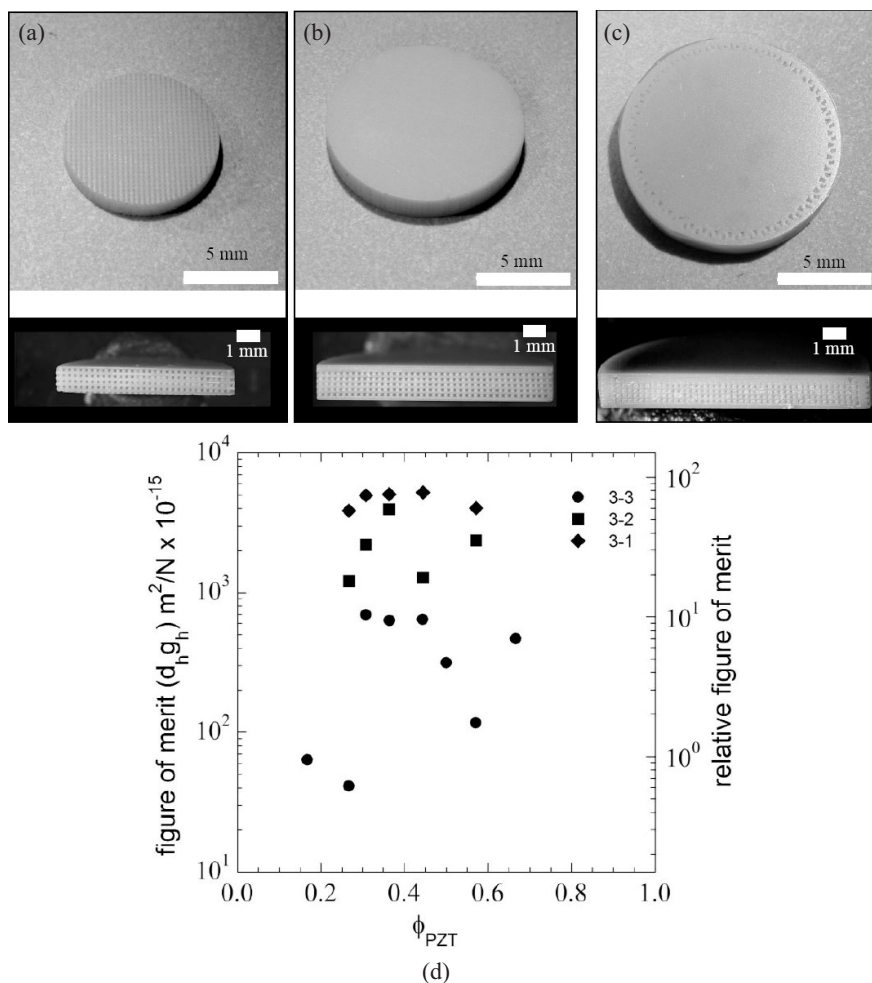
Figure 5. Optical images of the top (top row) and cross-sectional (middle row) views of a) 3–3, b) 3–2, and c) 3–1 PZT composites after polymer infiltration and machining. [Note: Each of these composite architectures contains 60 vol.-% PZT.] d) Semilog plot of the hydrostatic figure of merit ($\bar{d}_h\bar{g}_h$) for 3–3 (●), 3–2 (■), and 3–1 (▲) composites as a function of PZT volume fraction (ϕ_{PZT}). Reproduced with permission from [14]. Copyright 2002 (American Institute of Physics).

3. Fugitive Organic Inks for Direct Writing of 3D Microvascular Networks

3.1. Ink Design and Rheology

Wax-based materials serve as excellent fugitive inks for direct writing of 3D microvascular networks. First, these inks must flow through a fine deposition nozzle under high shear, yet be self-supporting under ambient conditions, even as they span gaps in the underlying layer(s). Second, the ink scaffold must maintain its shape during resin infiltration and curing. Finally, the ink scaffold must liquefy at modest temperatures to facilitate its removal from the polymer matrix, leaving behind an interconnected network of microchannels, in a process akin to the lost-wax technique.[7]

We developed a fugitive organic ink based on a binary mixture of microcrystalline wax ($M_w = 1450$ g mol^{-1}) and a low-molecular-weight organic phase ($M_w = 840$ g mol^{-1}) for direct-write assembly.[25] The ink elasticity, as characterized by the plateau value of the storage shear modulus (G'), increased linearly from ca. 0.1 to 1 MPa with increasing weight fraction of microcrystalline wax (data not shown). Figure 6a shows a plot of ink elasticity as a function of shear stress for the binary organic ink (40 wt % microcrystalline wax). As a benchmark, we include the data obtained for a commercial organic paste (Prussian blue paste, Loctite) used previously for microvascular network printing.[7] Both the G' and τ_y values observed for the binary organic ink exceed those reported for the commercial organic ink by more than an order of magnitude under ambient conditions. As a result of its superior mechanical properties, the binary ink enables the fabrication of microvascular networks composed of more than 100 layers with longer spanning filaments.

The time-dependent relaxation behavior of each fugitive ink was studied by optically imaging freestanding ink filaments (ca. 1 mm in diameter) produced by direct writing.[25] Representative optical images of ink filaments spanning a 10 mm gap are shown in Figure 6b for both the binary and commercial organic inks. As is evident in Figure 6b, the binary ink filament experiences significantly less deformation over the experimental timescale probed relative to the filament produced from the commercial ink. Their mid-span deflection as a function of time, shown in Figure 6b, was quantified by image analysis. Both inks displayed similar deformation behavior with an initially high deflection rate followed by gradual retardation before reaching a constant, lower deflection rate. Ultimately, the ink recovers to its plateau G' value, as revealed by the onset of a reduced deflection rate at longer times (≥ 10 s).

3.2. Direct-Write Assembly of 3D Microvascular Networks

3D microvascular networks may find potential application in microfluidic systems being developed for a broad range of technological applications, including biotechnology,[38] fluidic-based computers,[39] sensors,[40] chemical reactors[41] and autonomic materials.[42,43] We create these structures by depositing[12,15,22,32] a fugitive ink through a cylindrical nozzle (150 μm in diameter) onto a moving *x–y* platform (deposition speed of 6 mm s^{-1}). After the initial layer is generated, the platform is incremented in the *z*-direction and another layer is deposited. This process is repeated until the desired 3D ink scaffold is fabricated (see Fig. 7a). The interstitial pore space between patterned filamentary features is then infiltrated with a liquid resin consisting of 2.5:1 epoxide (EPON 828, Shell Chemicals)
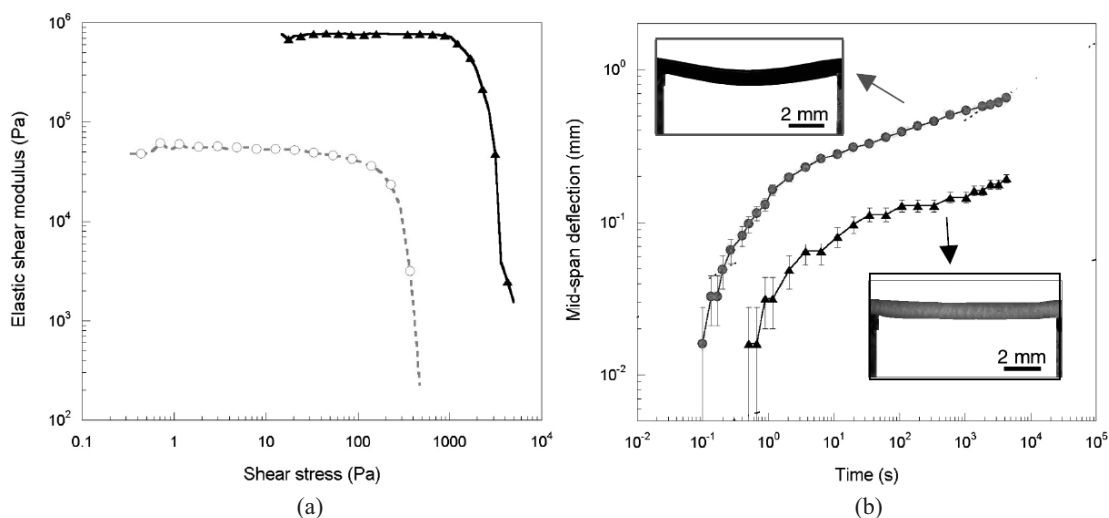
Figure 6. a) Log–log plot of shear elastic modulus as a function of shear stress for the binary organic ink (filled symbols, 40 wt % microcrystalline wax) and the commercial organic ink (open symbols). b) Plot of mid-span deflection as a function of time for the binary organic ink (black symbols) and commercial organic ink (grey symbols), along with optical images (side view) of the corresponding spanning filaments (150 µm rod diameter and 10 mm rod length) held for ca. 1 h at 20 °C. Reproduced with permission from [23].
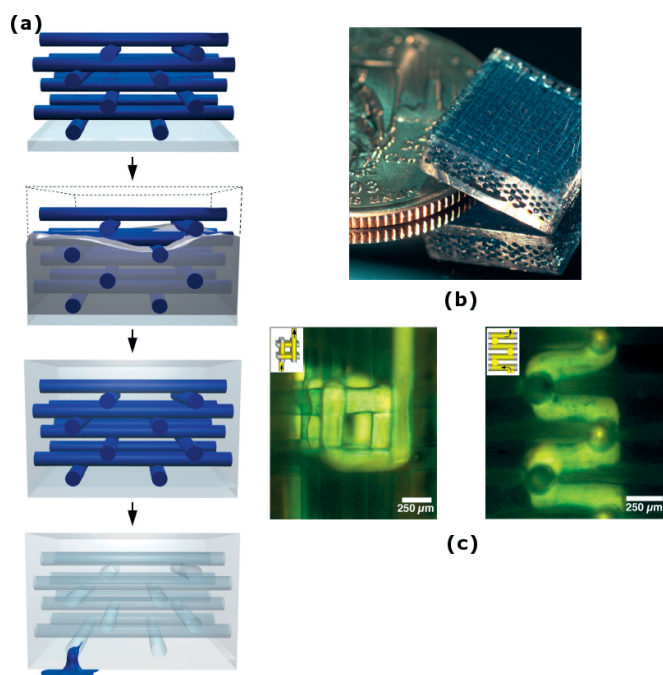

Figure 7. a) Schematic representation of the fabrication procedure for 3D microvascular networks showing (from top to bottom) the multilayer scaffold after ink deposition, resin infiltration into scaffold, resin curing to form structural matrix, and ink removal to yield an interconnected microvascular network. b) Optical image of a representative 3D microvascular network (16 layers, 200 µm diameter microchannels) created by this procedure. c) Fluorescent images (top and side views) of a square-spiral mixing element patterned within the network. Reproduced with permission from [7]. Copyright 2003 (Nature Publishing Group).

and cured for 24 h at 22 °C followed by 2 h at 60 °C. At this temperature, the ink scaffold liquefies and can be removed under light vacuum to yield an interconnected 3D network of hydrophilic microchannels (see Fig. 7b).

Highly efficient fluid-mixing devices, such as square-[7] and triangular-spiral[23] towers, can be embedded within these 3D microvascular networks using standard photomasking techniques. These mixing elements were introduced into this 3D network by first infiltrating the microchannels with a photocurable resin (Model 61, Norland Products) followed by subsequent patterning and UV flood exposure (360 nm wavelength for 60 s at 100 W). After the photopolymerization, the unreacted resin was drained under a light vacuum leaving behind the desired patterned features (see Fig. 7c).

The mixing efficiency of the 3D square-spiral towers was characterized by monitoring the mixing of two fluid streams that contain red and green fluorescent dyes (0.60 mg mL^{-1} of water, Bright Dyes), respectively, using fluorescent microscopy as a function of varying Reynolds number ($Re = Ul/v$, where U is the average flow speed, l is the characteristic cross-sectional dimension of the channel, and v is the kinematic viscosity of the fluid). Fluid mixing was also characterized in two alternate microfluidic devices: a straight (1D) microchannel and a square wave (2D) microchannel as shown in Figure 8, respectively. After the two fluid streams come into contact, the red and green fluorescent dyes begin to diffuse, resulting in the formation of a yellow (mixed) fluid layer (see Fig. 9a–c) 1D. Mixing occurs solely by molecular diffusion in the 1D device,[7] which serves as a benchmark for evaluating mixing efficiency of both the 2D and 3D devices.

To quantify the degree of mixing $\bar{I}$, the average yellow intensity $\langle I \rangle$ was measured across a given microchannel and compared to the intensity obtained when the two fluids were completely mixed $\langle I_{\mathrm{mix}} \rangle$ prior to their introduction to the channel. The relative intensity $\langle I \rangle = \langle I \rangle / \langle I_{\mathrm{mix}} \rangle$, where $\langle \rangle$ denotes the average taken over all pixels imaged in a given microchannel segment, ranges from 0 (unmixed) to 1 (fully mixed). This value is plotted as a function of Re in Figure 9d for each microfluidic device. The degree of mixing arising solely from diffusion under
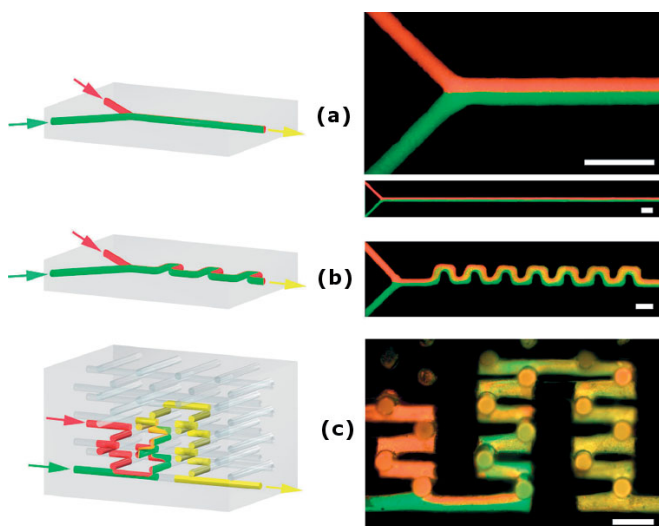
Figure 8. Schematic representations and fluorescence microscopy images of the 1D, 2D, and 3D microfluidic devices, where two fluids (red and green) are mixed at $Re = 30.6$ to produce the yellow (mixed) output. The arrows on schematics indicate the flow direction. The two fluids meet at a Y-junction where they enter a a) 17 mm straight microchannel and b) 15 mm (streamwise) square-wave microchannel. c) The two fluids are injected at discrete points within a 3D spiral tower before mixing within a series of two interconnected towers. All scale bars = 0.5 mm. Reproduced with permission from [7]. Copyright 2003 (Nature Publishing Group).

Figure 9. a–c) Color-filtered optical images show the yellow mixed zone inside the 1D (top, streamwise distance shown = 13–16 mm), 2D (middle, streamwise distance shown = 10–16 mm), and 3D (bottom, streamwise distance shown = 0–14 mm) microfluidic devices at low, intermediate, and high flow rates: a) $Re = 0.8$, b) $Re = 7.6$, and c) $Re = 30.6$. Scale bars = 250 μm. d) Degree of mixing at the output (streamwise distance = 14 mm) for the 1D (black), 2D (blue), and 3D (red) microfluidic devices at different Reynolds numbers. Mixing within the 3D device exhibits an exponential dependence on Re, where $\bar{I} = 1 - \exp(-\beta Re)$ and $b = 0.354$ above $Re \approx 1$. [Inset: The length of channel required to achieve 90% mixing ($\bar{I} = 0.9$) plotted versus natural logarithm of Re (and Pe). Reproduced with permission from [7]. Copyright 2003 (Nature Publishing Group).

pure laminar flow conditions (1D device) decreased rapidly with increasing Re, as the residence time was reduced within the channel. Mixing in the 2D device was diffusion dominated[7] at low Re before increasing linearly above $Re \sim 10$ (see Fig. 9d). Complete mixing was not observed for the 2D device until $Re \sim 70$. The mixing performance for the 3D microfluidic device was superior to the 1D and 2D cases over all Re investigated.[7] At low Re, diffusive mixing dominated leading to a decrease in relative intensity as Re increased from 0.15 to ca. 1.0. At higher Re, mixing was greatly accelerated due to chaotic advection and nearly complete mixing was achieved at $Re > 15$. The relative intensity approached unity (fully mixed) at an exponential rate for the 3D square-spiral towers above this transition (see Fig. 9d), since the timescale for homogenization grows with natural log of the Péclet number[44] (i.e., $t_{hom} \propto \ln(Pe)$).

Direct ink writing opens up new avenues for microfluidic device design that are inaccessible by conventional lithographic methods. Moreover, our approach is amenable to a wide range of matrix materials (e.g., epoxies, polydimethylsiloxane (PDMS), and hydrogels). While the benefits of using 3D microvascular networks as a basis for fluidic devices have been demonstrated, we envision that such networks could be applied more broadly. For example, combined with self-healing functionality,[43] a 3D microvascular network provides an analog to the human circulatory system for the next generation of autonomic healing materials. The embedded network would serve as a circulatory system for the continuous transport of repair chemicals to the site of damage within the material. In addition, such structures may also find potential application as self-cooling materials[45] or scaffolds for tissue engineering.[9]
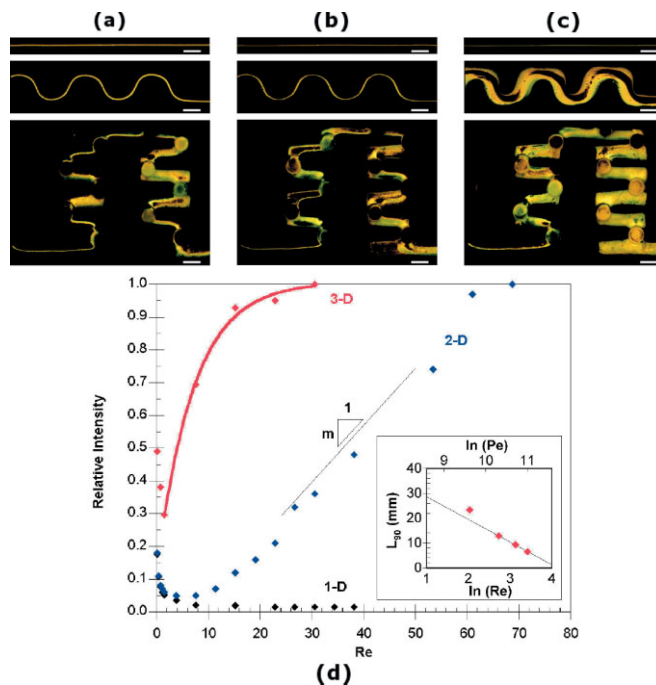
4. Polyelectrolyte Inks for Direct Writing of 3D Microperiodic Scaffolds

4.1. Ink Design and Rheology

It has been a grand challenge to design concentrated inks suitable for direct writing at the microscale. Viscoelastic inks, such as the colloidal gels or fugitive organic inks described above, either experience jamming (or clogging) in the deposition nozzle or require exceedingly large pressures to induce ink flow. Prior to our efforts,[12,15,22,32] Nature provided the only example of "direct ink writing" of complex structures with micrometer-sized, self-supported features, in the form of spider webs. Spiders create their webs by depositing a concentrated protein solution referred to as "spinning dope".[46] This low-viscosity fluid undergoes solidification as it flows through a fine-scale spinneret to form silk filaments.[46] Depending on the type of spider, filament diameters ranging from 10 nm to 10 μm have been observed.[46] Even though this process is difficult to mimic, spinning dope has been recently harvested from spiders[47] or grown by bacteria[48] and formed into silk filaments via deposition into a coagulation reservoir. We drew inspira-

tion from these natural and regenerative processes to develop concentrated polyelectrolyte complexes that, while less structurally complicated than spider silk, are specifically tailored for direct ink writing of 3D microperiodic scaffolds.

Our ink design utilizes polyelectrolyte complexes comprising non-stoichiometric mixtures of polyanions and polycations.[49] We first explored mixtures of poly(acrylic acid), PAA ($M_w = 10\,000$ g mol^{-1}) and poly(ethylenimine), PEI ($M_w = 600$ g mol^{-1}) that were nominally 40 wt % polyelectrolyte in an aqueous solution. By regulating the ratio of anionic (COONa) to cationic (NH$_x$) groups and combining these species under solution conditions that promote polyelectrolyte exchange reactions,[50] we produced homogeneous fluids over a broad compositional range that possessed the requisite viscosities (see Fig. 10a) needed to facilitate their flow through microcapillary nozzles of varying diameter ($D = 0.5$–5.0 µm).
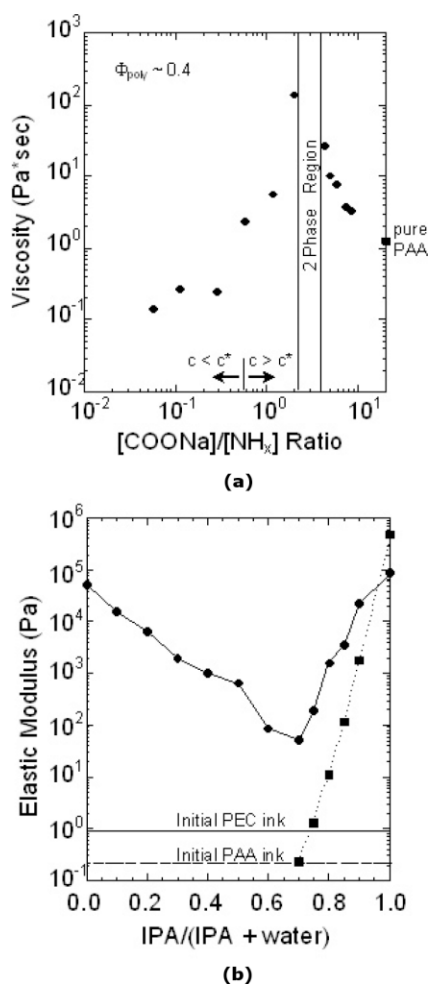

Figure 10. a) Log–log plot of solution viscosity as a function of varying [COONa:NH$_x$] ratio for PAA/PEI inks (40 % w/w). As a benchmark, the viscosity of a concentrated PAA solution (40 wt %) is shown on the right axis. b) Semi-log plot of the equilibrium elastic modulus of the PAA/PEI ink (40 wt % with a 5.7:1 [COONa:NH$_x$] ratio) coagulated in reservoirs of varying composition for PAA/PEI ink (circles) and a pure PAA ink (40 wt.-%) (squares). Reproduced with permission from [24]. Copyright 2006 (American Chemical Society).

These concentrated polyelectrolyte inks rapidly coagulate to yield self-supporting filaments (or rods) upon deposition into an alcohol/water coagulation reservoir. The exact coagulation mechanism, driven by electrostatics in a water-rich reservoir, or solvent-quality effects in an alcohol-rich reservoir, as well as the magnitude of ink elasticity, depend strongly on reservoir composition.[24] As shown in Figure 10b, the PAA/PEI ink ([COONa]/[NH$_x$] = 5.7) exhibits a dramatic rise in ink elasticity from 1 Pa (fluid phase) to nearly 10^5 Pa (coagulated phase) in a reservoir containing 83–88 % isopropyl alcohol. Under these conditions, the deposited ink filament is elastic enough to promote shape retention, yet maintains sufficient flexibility for continuous flow and adherence to the substrate and underlying patterned layers. This ink design can be extended other polyelectrolyte mixtures,[4] including those based on biologically, electrically, or optically active species.

4.2. Direct-Writing of 3D Polyelectrolyte Scaffolds

3D microperiodic polyelectrolyte structures may find potential application as sophisticated scaffolds that guide the electrostatic layer-by-layer assembly of materials,[51] direct cell-scaffold interactions,[52] or interact with other environmental stimuli,[6] or as templates for biomimetic,[25] photonic,[26] microfluidic,[7,23] or low-cost microelectromechanical devices (MEMs).[53] The development of a fluid ink that flows through fine deposition nozzles, and then rapidly solidifies in a coagulation reservoir is central to our ability to pattern these structures at the microscale. As the ink exits the nozzle, it forms a continuous, rodlike filament that retains its shape after rapid coagulation in the deposition reservoir (see Fig. 11a and b). A representative 3D lattice and radial array assembled by our technique are shown in Figure 11c. They possess features that are nearly two orders of magnitude smaller than those attained by other multilayer ink printing techniques.[4,54] Such scaffolds can be assembled with arbitrary shapes, including those with solid or porous walls, spanning (rodlike) filaments, and tight or broad angled features, revealing the flexibility of our approach (see Fig. 11).

4.3. 3D Polyelectrolyte Scaffolds: Templates for Photonic Structures

Since the concept of a photonic bandgap (PBG)[55] was first introduced, there has been intense interest in generating 3D microperiodic structures comprised of alternating high- and low-refractive-index materials.[8] Si is an ideal material for photonic crystals, because it has a high refractive index ($n \sim 3.45$) and is optically transparent in the infrared. The woodpile structure,[56] which consists of a 3D array of orthogonally stacked rods, is particularly well suited for direct-write assembly.[57] Both ink-[11] and laser-writing[2,57] approaches provide rapid flexible routes for fabricating such structures. However, these approaches are currently limited to polymeric structures that lack the high-refractive-index contrast and mechanical integrity required for many applications. To overcome this limitation, we recently developed a replication (or templating)
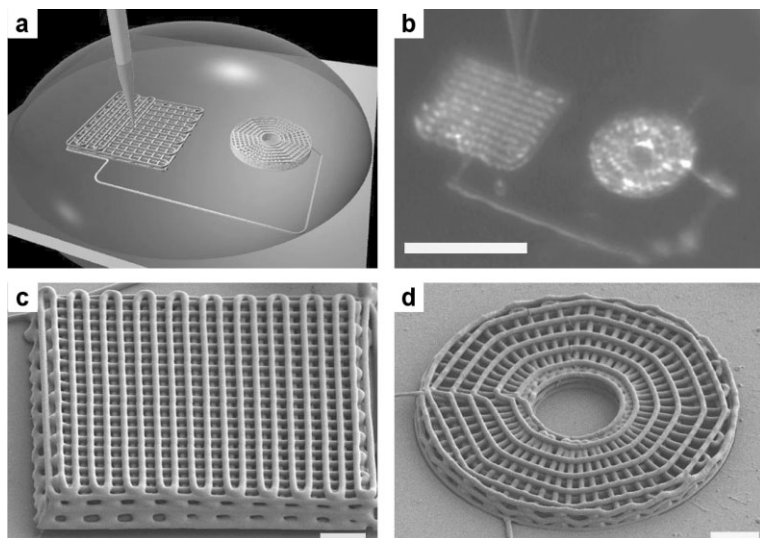
Figure 11. a) Schematic illustration of the ink deposition process (not drawn to scale). A concentrated polyelectrolyte ink is housed in the syringe (shown in yellow) immersed in a coagulation reservoir (grey hemispherical drop) and deposited onto a glass substrate (shown in light grey). b) Optical image acquired in situ during deposition reveals the actual features illustrated in (a) including the deposition nozzle that is currently patterning a 3D periodic lattice, and an image of a completed 3D radial array alongside this structure. This image is blurred, because the imaged features reside within the coagulation reservoir. c) 3D periodic lattice with a simple tetragonal geometry (8 layers, 1 μm rod diameter). d) 3D radial array (5 layers, 1 μm rod diameter). Adapted with permission from [4]. Copyright 2004 (Nature Publishing Group).

scheme that enables their structural conversion to 3D Si hollow-woodpile structures via a sequential silica[58]/Si[59] chemical vapor deposition (CVD) process.[49] In related work, Ozin and co-workers[60] have demonstrated that this approach is also suitable for converting the polymeric scaffolds produced by direct laser writing into Si woodpile structures.

3D polymer woodpiles are fabricated by direct writing a concentrated polyelectrolyte ink in a layer-by-layer build sequence[4] (Fig. 12). Both 8- and 16-layer woodpile structures ranging in lateral dimensions from 250 μm × 250 μm to 500 μm × 500 μm were formed with in-plane center-to-center rod spacings (*d*) of 2.8 μm and 4.0 μm, and a rod diameter of 1 μm.[49] Note, these values do not represent process limits, as the maximum lateral dimensions may exceed 1 cm × 1 cm, rod diameters can be as low as 600 nm, and the rods can be close-packed with a pitch that equals the rod dimension.[4,24]

To generate a structure with strong photonic effects, it is necessary to enhance the refractive-index contrast, for example, by infilling some of the void space with Si. Because the polymer scaffolds cannot withstand the high-temperature conditions necessary for Si CVD, a sequential deposition step is required. First, the polymer woodpile structure is coated with a ca. 100 nm thick layer of silica (SiO_2) via a room-temperature CVD process.[61] In this step, water vapor was flowed over the sample for 90 s to hydrate its surface prior to introducing a stream of $SiCl_4(g)$-saturated nitrogen gas that passed over the structure at 6 mL min^{-1} for 90 s. Note, there is a rather narrow reaction window for optimal silica coverage. The polymer is subsequently removed by heating the sample at 475 °C in air

for 3 h. This results in a SiO_2 hollow woodpile structure that can now withstand the processing temperatures required for Si CVD. A ca. 100 nm thick layer of Si is then deposited on both the inner and outer walls of the SiO_2 tubular array via CVD of disilane (Si_2H_6) as the precursor gas.[62] Because the initial polymer scaffold is interconnected in all three dimensions, the resulting hollow-woodpile structure formed after SiO_2/Si CVD is composed of an interconnected array of cylinders that possess a total wall thickness of ~ 300 nm (see Fig. 12).[49]

The intensity and spectral position of the optical features from polymer and hollow-woodpile structures depend strongly on their geometry and composition. The influence of each processing step on their optical properties is illustrated in Figure 13. Upon silica deposition, the reflectance peaks of the SiO_2/polymer woodpile shift to longer wavelengths, because the additional material increases its average refractive index. Essentially, a small fraction of the air voids within the structure are replaced with silica. The dramatic blue-shift of the optical features upon polymer removal stems from the significant reduction in the average refractive index, as the polymer is now replaced with air. Following Si CVD, a remarkable red-shift is observed in the diffraction peaks due to an increase in its average refractive index. Finally, the silica scaffold was removed through HF etching, resulting in a slight blue-shift of the diffraction peaks. We view these preliminary results as quite promising despite the relatively low reflectivity values observed for the Si hollow-woodpile structure.[49] Further refinements of their architecture and subsequent materials-processing steps are now underway to optimize their optical properties. Along with photonic applications, these structures may serve as a novel starting point for other potential applications, including Si-based microfluidic networks and low-cost MEMs, where their hollow nature may be ideal for heat-transfer applications and reduced inertial forces.

4.4. 3D Polyelectrolyte Scaffolds: Templates for Biomimetic Mineralization

Building on the recent discovery that both natural[63] and synthetic polyamines[64,65] catalyze the hydrolysis and condensation of silica precursors under ambient conditions, we developed a novel approach for templating 3D hybrid silica–organic structures that combines direct ink writing with biomimetic silicification.[25] These structures may be considered as synthetic analogs to naturally occurring diatom frustules. We created a polyamine-rich ink, composed of poly(allylamine hydrochloride) (PAH, $M_w = 60\,000$ g mol^{-1}) and PAA ($M_w = 10\,000$ g mol^{-1}) with a [NH$_x$]/[COONa] ratio of 2, which is capable of being both patterned by direct writing and subsequently mineralized. The relative ease with which we were able to produce cationic-rich mixtures with significantly higher molecular weights those than anionic-rich inks described above illustrates the generality of our approach.
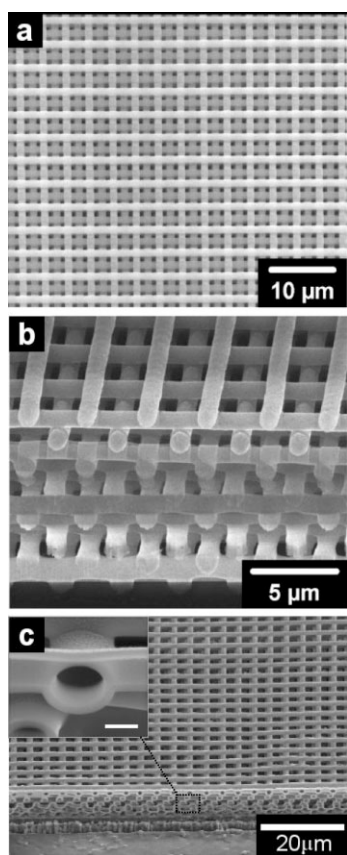
Figure 12. a) SEM image of polyelectrolyte woodpile (16 layers, 4 μm in-plane pitch, 1 μm rod diameter) assembled by direct ink writing (top view), b) focused ion beam milled cross section showing the excellent alignment between layers, and c) SEM image of a Si/SiO₂/Si hollow-woodpile structure after focused ion beam milling (inset corresponds to higher magnification view of the interconnected hollow rods). Adapted with permission from [26].
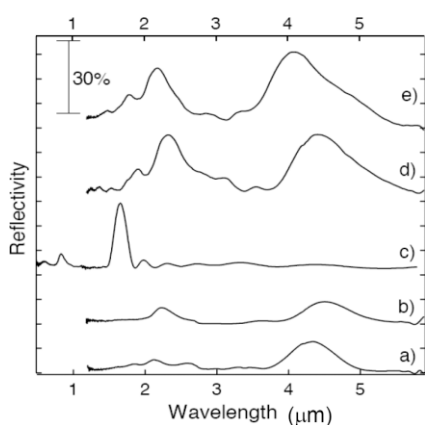

Figure 13. Reflectance spectra for a 3D microperiodic structure (8 layers, 2.8 μm in-plane pitch, 1 μm rod diameter). a) Polymer woodpile, b) SiO_2/polymer woodpile, c) SiO_2 hollow woodpile, d) Si/SiO_2/Si hollow-woodpile, e) Si hollow woodpile after HF etch. Reproduced with permission from [26].

We explored the silicification of polyamine-rich scaffolds using either a single or sequential immersion method under ambient conditions. The first method is similar to prior in vitro experiments, in which silica nanoparticles formed rapidly via an amine-mediated mechanism[64,66] upon exposing a polyamine solution to a phosphate-buffered, silicic acid solution. In the second method, the scaffolds are first exposed to a silicic acid solution followed by exposure to a phosphate-buffered solution with the aim of enhancing the mineralization process. We found that in order to preserve their intricately patterned shapes, the scaffolds must first be heated to 180 °C to induce partial crosslinking between the PAH and PAA chains through amide bond formation.[67] Partially crosslinked scaffolds that were silicified via the single immersion method possessed a rather low silica content (ca. 11 wt %), as shown in Figure 14. In great contrast, those that underwent sequential immersion exhibited a nearly fivefold increase in their silica content (ca. 52 wt %) for identical immersion times (48 h). Under these conditions, silica condensation occurs uniformly throughout these scaffolds leading to their enhanced thermal and mechanical stability.[25] As a result, their shape is preserved with high precision even when the organic phase is fully removed by heating them to 1000 °C (see Fig. 14). Note, the twofold decrease in their overall size is in good agreement with the dimensional changes expected based on their initial silica content after mineralization.
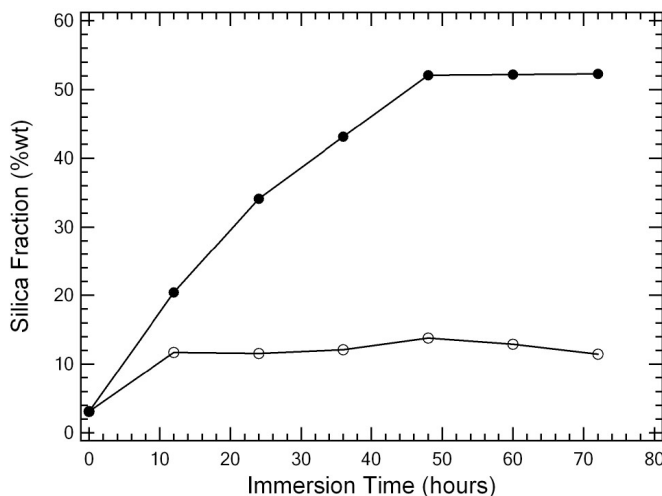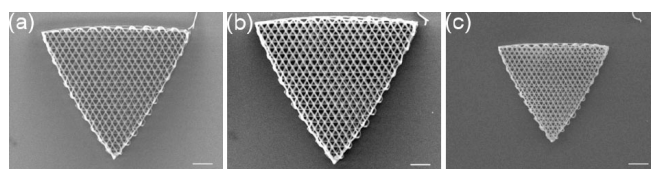
Figure 14. SEM images of triangular-shaped polyelectrolyte scaffolds showing their structural evolution: a) as-patterned scaffold, b) partially crosslinked scaffold after silicification by the sequential immersion method, and c) silica scaffold after heat treatment at 1000 °C. (All scale bars 20 μm.) d) The silica content (wt % of total mass) as a function of immersion time for both the single (open symbols) and sequential immersion methods (filled symbols). Adapted with permission from [25]. Copyright 2006 (Royal Society of Chemistry).

As recently demonstrated for natural diatom frustules, we anticipate that these silicified structures can be readily converted to other materials, such as MgO[68] or titania[69] through a halide gas/solid displacement reaction. More generally, our ink design can be extended to incorporate natural or synthetic polypeptides that allow a broader range of biomineralization strategies to be pursued, which when coupled with our ability to pattern 3D structures of arbitrary shape and periodicity, may open up new avenues for soft-to-hard matter conversion under ambient conditions.

5. Opportunities and Challenges

Direct ink writing offers the ability to rapidly pattern functional materials in complex 3D architectures from a broad array of materials. The continual drive towards patterning materials at even finer length scales and faster printing speeds gives rise to many opportunities and challenges. Future advances will require new ink designs, better characterization and modeling of ink dynamics during deposition, and enhanced robotic-control and ink-delivery systems to allow 3D writing with greater precision and local composition specificity.

We are currently exploring several new designs, including inks based on biphasic colloidal mixtures, hydrogels, and sol–gel precursors with the above objectives in mind. Using techniques such as microparticle imaging velocimetry, we are able to directly measure the flow profiles of these inks within model deposition nozzles. We are also investigating multimaterial and reactive ink deposition, which require the integration of efficient mixing strategies within the deposition nozzle at the microscale. The ability to locally specify both composition and structure will allow even greater control over the properties and functionality of the resulting patterned materials. Finally, if 3D direct ink writing approaches are to move from prototyping to large-scale production, more sophisticated print heads must be implemented, such as those based on microfluidic devices and/or multinozzle arrays, to enable the simultaneous creation of several components from a given printing platform. Given the rapid development thus far, direct ink writing appears poised to deliver the next generation of designer materials for a wide range of technological applications.

[1] A. van Blaaderen, R. Ruel, P. Wiltzius, *Nature* **1997**, *385*, 321.
[2] B. H. Cumpston, S. P. Ananthavel, S. Barlow, D. L. Dyer, J. E. Ehrlich, L. L. Erskine, A. A. Heikal, S. M. Kuebler, I. Y. S. Lee, D. McCord-Maughon, J. Qin, H. Rockel, M. Rumi, X.-L. Wu, S. R. Marder, J. W. Perry, *Nature* **1999**, *398*, 51.
[3] M. Campbell, D. N. Sharp, M. T. Harrison, R. G. Denning, A. J. Turberfield, *Nature* **2000**, *404*, 53.
[4] G. M. Gratson, M. Xu, J. A. Lewis, *Nature* **2004**, *428*, 386.
[5] S. Y. Lin, J. G. Fleming, D. L. Hetherington, B. K. Smith, R. Biswas, K. M. Ho, M. M. Sigalas, W. Zubrzycki, S. R. Kurtz, J. Bur, *Nature* **1998**, *394*, 251.
[6] Y. J. Lee, P. V. Braun, *Adv. Mater.* **2003**, *15*, 563.
[7] D. Therriault, S. R. White, J. A. Lewis, *Nat. Mater.* **2003**, *2*, 265.
[8] J. D. Joannopoulos, P. R. Villeneuve, S. H. Fan, *Nature* **1997**, *386*, 143.
[9] L. G. Griffith, G. Naughton, *Science* **2002**, *295*, 1009.
[10] Y. Y. Li, F. Cunin, J. R. Link, T. Gao, R. E. Betts, S. H. Reiver, V. Chin, S. N. Bhatia, M. J. Sailor, *Science* **2003**, *299*, 2045.
[11] J. A. Lewis, G. M. Gratson, *Mater. Today* **2004**, *7*, 32.
[12] J. Cesarano, P. Calvert, *US Patent 6 027 326*, **2000**.
[13] J. Cesarano, R. Segalman, P. Calvert, *Ceram. Ind.* **1998**, *184*, 94.
[14] J. E. Smay, J. Cesarano, B. A. Tuttle, J. A. Lewis, *J. Appl. Phys.* **2002**, *92*, 6119.
[15] J. E. Smay, J. Cesarano, J. A. Lewis, *Langmuir* **2002**, *18*, 5429.
[16] S. L. Morissette, J. A. Lewis, P. G. Clem, J. Cesarano, D. B. Dimos, *J. Am. Ceram. Soc.* **2001**, *84*, 2462.
[17] G. M. Lous, I. A. Cornejo, T. F. McNulty, A. Safari, S. C. Danforth, *J. Am. Ceram. Soc.* **2000**, *83*, 124.
[18] D. W. Hutmacher, T. Schantz, I. Zein, K. W. Ng, S. H. Teoh, K. C. Tan, *J. Biomed. Mater. Res.* **2001**, *55*, 203.
[19] E. Sachs, M. Cima, P. Williams, D. Brancazio, J. Cornie, *J. Eng. Ind. Trans. ASME* **1992**, *114*, 481.
[20] a) J. H. Song, M. J. Edirisinghe, J. R. G. Evans, *J. Am. Ceram. Soc.* **1999**, *82*, 3374. b) M. Mott, J. R. G. Evans, *Mater. Sci. Eng. A* **1999**, *271*, 344. c) B. Y. Tay, M. J. Edirisinghe, *J. Mater. Res.* **2001**, *16*, 373.
[21] K. A. M. Seerden, N. Reis, J. R. G. Evans, P. S. Grant, J. W. Halloran, B. Derby, *J. Am. Ceram. Soc.* **2001**, *84*, 2514.
[22] J. E. Smay, G. M. Gratson, R. F. Shepherd, J. Cesarano, J. A. Lewis, *Adv. Mater.* **2002**, *14*, 1279.
[23] D. Therriault, R. F. Shepherd, S. R. White, J. A. Lewis, *Adv. Mater.* **2005**, *17*, 395.
[24] G. M. Gratson, J. A. Lewis, *Langmuir* **2005**, *21*, 457.
[25] M. Xu, G. M. Gratson, E. B. Duoss, R. F. Shepherd, J. A. Lewis, *Soft Matter* **2006**, *2*, 205.
[26] G. M. Gratson, F. Garcia-Santamaria, V. Lousse, M. J. Xu, S. H. Fan, J. A. Lewis, P. V. Braun, *Adv. Mater.* **2006**, *18*, 461.
[27] J. J. Guo, J. A. Lewis, *J. Am. Ceram. Soc.* **1999**, *82*, 2345.
[28] G. M. Channell, K. T. Miller, C. F. Zukoski, *AIChE J.* **2000**, *46*, 72.
[29] W. Herschel, B. Bulkley, *Kolloid* **1926**, *39*, 291.
[30] a) K. M. Kalyon, P. Yaras, B. Aral, U. Yilmazer, *J. Rheol.* **1993**, *37*, 35. b) R. Buscall, J. I. McGowan, A. J. Mortonjones, *J. Rheol.* **1993**, *37*, 621.
[31] R. B. Rao, K. L. Krafcik, A. M. Morales, J. A. Lewis, *Adv. Mater.* **2005**, *17*, 289.
[32] Q. Li, J. A. Lewis, *Adv. Mater.* **2003**, *15*, 1639.
[33] J. N. Stuecker, J. Cesarano, D. A. Hirschfeld, *J. Mater. Process. Technol.* **2003**, *142*, 318.
[34] G. He, D. A. Hirschfeld, J. C. Cesarano III., in *Proc. of 24th Int. Conf. & Exposition on Engineering Ceramics and Structures*, The American Ceramic Society, Westerville, OH **2000**, Paper No. C-071-00.
[35] S. Michna, W. Wu, J. A. Lewis, *Biomaterials* **2005**, *26*, 5632.
[36] J. E. Smay, J. Cesarano, B. A. Tuttle, J. A. Lewis, *J. Am. Ceram. Soc.* **2004**, *87*, 293.
[37] C. S. Marchi, M. Kouzeli, R. Rao, J. A. Lewis, D. C. Dunand, *Scr. Mater.* **2003**, *49*, 861.
[38] a) M. A. Burns, B. N. Johnson, S. N. Brahmasandra, K. Handique, J. R. Webster, M. Krishnan, T. S. Sammarco, P. M. Man, D. Jones, D. Heldsinger, C. H. Mastrangelo, D. T. Burke, *Science* **1998**, *282*, 484. b) A. Stromberg, A. Karlsson, F. Ryttsen, M. Davidson, D. T. Chiu, O. Orwar, *Anal. Chem.* **2001**, *73*, 126. c) H. P. Chou, A. Spence, A. Scherer, S. Quake, *Proc. Natl. Acad. Sci. USA* **1999**, *96*, 11. d) J.-W. Choi, C. H. Ahn, in *Proc. of Microfluidic Devices and Systems III*, Santa Clara, CA, USA, *4177*, 154, **2000**. SPIE.
[39] S. K. Moore, *IEEE Spectrum* **2001**, *38*, 28.
[40] M. L. Chabinyc, D. T. Chiu, J. C. McDonald, A. D. Stroock, J. F. Christian, A. M. Karger, G. M. Whitesides, *Anal. Chem.* **2001**, *73*, 4491.
[41] a) M. W. Losey, M. A. Schmidt, K. F. Jensen, *Ind. Eng. Chem. Res.* **2001**, *40*, 2555. b) N. L. Jeon, S. K. W. Dertinger, D. T. Chiu, I. S. Choi, A. D. Stroock, G. M. Whitesides, *Langmuir* **2000**, *16*, 8311.
[42] D. J. Beebe, J. S. Moore, J. M. Bauer, Q. Yu, R. H. Liu, C. Devadoss, B. H. Jo, *Nature* **2000**, *404*, 588.

[43] S. R. White, N. R. Sottos, P. H. Geubelle, J. S. Moore, M. R. Kessler, S. R. Sriram, E. N. Brown, S. Viswanathan, *Nature* **2001**, *409*, 794.

[44] S. W. Jones, in *Chaos Applied to Fluid Mixing* (Eds: H. Aref, M. S. El Naschie), Pergamon, Oxford, UK **1995**, p. 185.

[45] G. J. Snyder, J. R. Lim, C. K. Huang, J. P. Fleurial, *Nat. Mater.* **2003**, *2*, 528.

[46] F. Vollrath, D. P. Knight, *Nature* **2001**, *410*, 541.

[47] A. Seidel, O. Liivak, L. W. Jelinski, *Macromolecules* **1998**, *31*, 6733.

[48] A. Lazaris, S. Arcidiacono, Y. Huang, J. F. Zhou, F. Duguay, N. Chretien, E. A. Welsh, J. W. Soares, C. N. Karatzas, *Science* **2002**, *295*, 472.

[49] A. B. Zezin, V. A. Kabanov, *Russ. Chem. Rev.* **1982**, *51*, 833.

[50] A. Zintchenko, G. Rother, H. Dautzenberg, *Langmuir* **2003**, *19*, 2507.

[51] G. Decher, *Science* **1997**, *277*, 1232.

[52] C. S. Chen, M. Mrksich, S. Huang, G. M. Whitesides, D. E. Ingber, *Science* **1997**, *276*, 1425.

[53] T. Yamamoto, J. Yamaguchi, N. Takeuchi, A. Shimizu, R. Sawada, E. Higurashi, Y. Uenishi, *Jpn. J. Appl. Phys., Part 1* **2004**, *43*, 5824.

[54] D. B. Chrisey, *Science* **2000**, *289*, 879.

[55] a) E. Yablonovitch, *Phys. Rev. Lett.* **1987**, *58*, 2059. b) S. John, *Phys. Rev. Lett.* **1987**, *58*, 2486.

[56] a) K. M. Ho, C. T. Chan, C. M. Soukoulis, R. Biswas, M. Sigala, *Solid State Commun.* **1994**, *89*, 413. b) H. S. Sozuer, J. P. Dowling, *J. Mod. Opt.* **1994**, *41*, 231.

[57] M. Deubel, G. von Freymann, M. Wegener, S. Pereira, K. Busch, C. M. Soukoulis, *Nat. Mater.* **2004**, *3*, 444.

[58] H. Miguez, N. Tetreault, B. Hatton, S. M. Yang, D. Perovic, G. A. Ozin, *Chem. Commun.* **2002**, 2736.

[59] A. Blanco, E. Chomski, S. Grabtchak, M. Ibisate, S. John, S. W. Leonard, C. Lopez, F. Meseguer, H. Miguez, J. P. Mondia, G. A. Ozin, O. Toader, H. M. van Driel, *Nature* **2000**, *405*, 437.

[60] N. Tetreault, G. von Freymann, M. Deubel, M. Hermatschweiler, F. Perez-Willard, S. John, M. Wegener, G. A. Ozin, *Adv. Mater.* **2006**, *18*, 457.

[61] H. Miguez, S. M. Yang, N. Tetreault, G. A. Ozin, *Adv. Mater.* **2002**, *14*, 1805.

[62] F. Garcia-Santamaria, M. Ibisate, I. Rodriguez, F. Meseguer, C. Lopez, *Adv. Mater.* **2003**, *15*, 788.

[63] a) J. N. Cha, G. D. Stucky, D. E. Morse, *Nature* **2000**, *403*, 403. b) L. L. Brett, R. R. Naik, D. J. Pikas, S. M. Kirkpatrick, D. W. Tomlin, P. W. Whitlock, S. J. Clarsen, M. O. Stone, *Nature* **2001**, *413*, 291.

[64] H. Menzel, S. Horstmann, P. Behrens, P. Baernreuther, I. Krueger, M. Jahns, *Chem. Commun.* **2003**, 2994.

[65] S. V. Patwardhan, S. J. Clarson, *Silicon Chem.* **2002**, *1*, 207.

[66] a) G. Pohnert, *Angew. Chem. Int. Ed.* **2002**, *41*, 3167. b) N. Kroger, S. Lorenz, E. Brunner, M. Sumper, *Science* **2002**, *298*, 584.

[67] J. J. Harris, P. M. DeRose, M. L. Bruening, *J. Am. Chem. Soc.* **1999**, *121*, 1978.

[68] K. H. Sandhage, M. B. Dickerson, P. M. Huseman, M. A. Caranna, J. D. Clifton, T. A. Bull, T. J. Heibel, W. R. Overton, M. E. A. Schoenwaelder, *Adv. Mater.* **2002**, *14*, 429.

[69] R. R. Unocic, F. M. Zalar, P. M. Sarosi, Y. Cai, K. H. Sandhage, *Chem. Commun.* **2004**, 796.

_____